chemistry

MDPI

Article

Paddlewheel-Type Diruthenium(II) Naphthyridine Complex with Electron-Withdrawing Trifluoroacetate Ligands

Yusuke Kataoka *, Nozomi Tada, Junya Omaki, Kanami Matsubara, Natsumi Yano and Makoto Handa

Department of Chemistry, Graduate School of Natural Science and Technology, Shimane University, 1060, Nishikawatsu, Matsue 690-8504, Shimane, Japan

* Correspondence: kataoka@riko.shimane-u.ac.jp

Abstract: A ligand exchange reaction between $[Ru_2(npc)_2(O_2CMe)_2]$ (**1**; npc = 1,8-naphthyridine-2-carboxylate) and trifluoroacetic acid yielded the diruthenium naphthyridine complex with two trifluoroacetate ligands, $[Ru_2(npc)_2(O_2CCF_3)_2]$ (**2**), which was structurally characterized by electrospray ionization mass spectrometry, elemental analysis, infrared spectrum, and synchrotron single-crystal X-ray diffraction. The crystal structure of **2** adopts a paddlewheel-type structure in which two npc and two O_2CCF_3 ligands are coordinated in a *cis*-2:2 arrangement around the Ru_2 core. The temperature-dependent magnetic susceptibility measurements indicated that **2** has (i) an $S = 1$ spin state for the Ru_2^{4+} core and (ii) a large D value of 243 cm^{-1}; characteristic of paddlewheel-type Ru_2 complexes. The cyclic voltammetry measurements indicated that **2** exhibited one reversible oxidation wave ($E_{1/2}$ = 0.72 V vs. SCE) and two reduction waves ($E_{1/2}$ = −0.67 and −1.10 V vs. SCE); which were clearly positively shifted when compared with those of **1**. Additionally, the absorption spectrum of **2** displayed intense absorption bands in the visible region; attributed to metal-to-ligand charge transfer from the Ru_2 core to the npc ligands; which were blue-shifted by approximately 70–100 nm when compared with those of **1**. These distinct shifts in redox potentials and absorption bands originated from the strong electron-withdrawing effect of the O_2CCF_3 ligands in **2**.

Keywords: diruthenium complex; paddlewheel-type structure; crystal structure; magnetic property; absorption feature

Academic Editors: Xin Wu and Igor Alabugin

Received: 27 February 2025
Revised: 5 April 2025
Accepted: 23 April 2025
Published: 1 May 2025

Citation: Kataoka, Y.; Tada, N.; Omaki, J.; Matsubara, K.; Yano, N.; Handa, M. Paddlewheel-Type Diruthenium(II) Naphthyridine Complex with Electron-Withdrawing Trifluoroacetate Ligands. *Chemistry* **2025**, *7*, 72. https://doi.org/10.3390/chemistry7030072

1. Introduction

The paddlewheel-type dinuclear complexes, $[M_2(EL)_4(AL)_X]$ (EL = equatorial ligand, AL = axial ligand, x = 0–2), are one of the most well-known structural motifs in the field of polynuclear metal complexes [1–7]. This type of complex has been extensively investigated not only from the perspective of fundamental coordination chemistry, including molecular structure, metal–metal interactions, and multiple bonding but also for its applications such as functional secondary building units in metal-organic frameworks and its diverse functionalities arising from the selection of central metal ions [8–12]. Among these complexes, diruthenium (Ru_2) complexes [1,13–17] are particularly interesting because they are redox-active species capable of forming three oxidation states (Ru_2^{4+}, Ru_2^{5+}, and Ru_2^{6+}). Their rich oxidation states and the multiple Ru–Ru bonds endow them with intriguing functionalities, including molecular magnetism [18–21], catalysis [22–25], antitumor activity [26,27], and electrochromism [28]. The oxidation state of this type of Ru_2 complex is greatly influenced by the type of bridging ligand; carboxylates, the most extensively studied bridging ligands, are known to stabilize the Ru_2^{5+} oxidation state with a quartet

(S = 3/2) spin state in air [1,29]. By contrast, the Ru_2^{4+} and Ru_2^{6+}, which have a triplet (S = 1) spin state, are generally unstable in air, and only a limited number of bridging ligands can stabilize these oxidation states under ambident conditions [1,30,31].

Based on this background, we recently developed a 1,8-naphthyridine-2-carboxylate (npc)-bridged Ru_2^{4+} complex $[Ru_2(npc)_2(O_2CMe)_2]$ (**1**; Scheme 1), which is air-stable in both the solid and solution states [32]. Single crystal X-ray diffraction (SCXRD) analyses revealed that **1** forms a paddlewheel-type structure in which two npc and two acetate ligands coordinate to the Ru_2 core in a *cis*-2:2-arrangement. In this structure, the naphthyridine moieties and carboxyl groups of npc ligands coordinate to the Ru_2 core at the equatorial and axial positions, respectively. Density functional theory (DFT) calculation clarified that the highest-occupied molecular orbital (HOMO) and lowest-unoccupied MO (LUMO) of **1** are localized on the δ* (Ru_2) and π* (npc) orbitals, respectively. Owing to its MO configuration, **1** exhibited the intense metal-to-ligand charge transfer (MLCT) transitions from the Ru_2 core to the npc ligands in the visible light region, which were not typically observed in carboxylate-bridged paddlewheel-type Ru_2 complexes. Additionally, reacting **1** with an excess amount of benzoic acid selectively replaced the acetate ligands of **1**, yielding $[Ru_2(npc)_2(O_2CC_6H_5)_2]$ with a high yield. In general, the absorption and redox properties of paddlewheel-type Ru_2 complexes drastically change when electron-withdrawing or donating groups are introduced into the bridging-carboxylate moieties [33–36]. For example, Ru_2 complexes with electron-withdrawing trifluoroacetate as bridging ligands [37] are expected to exhibit a positive shift in redox potential and a blue shift in absorption due to the stabilization of MOs of Ru_2 cores.

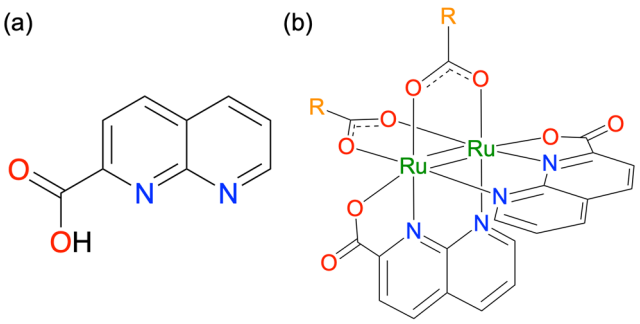

Scheme 1. Molecular structures of (**a**) Hnpc and (**b**) $[Ru_2(npc)_2(O_2CR)_2]$.

In this study, a paddlewheel-type Ru_2 naphthyridine complex with trifluoroacetate bridging ligands, $[Ru_2(npc)_2(O_2CCF_3)_2]$ (**2**), was synthesized and characterized by electrospray ionization mass spectroscopy (ESI-MS), infrared spectrum, elemental analysis, and SCXRD analysis. The electrochemical and absorption spectral properties of **2** were investigated, and their results were compared with those of **1**. Furthermore, DFT and time-dependent DFT (TDDFT) calculations were also performed to clarify the electronic features of **2** in detail.

2. Materials and Methods

2.1. Chemicals and Instruments

Complex **1** was synthesized according to a literature procedure [32]. 1,8-naphthyridine-2-carboxylic acid (Hnpc) was purchased from ChemScene LLC (Monmouth Junction, NJ, USA), and trifluoroacetic acid was purchased from Kanto Chemical Co. (Tokyo, Japan). All other chemicals were purchased from Fujifilm-Wako Pure Chemical Industry (Osaka, Japan).

Positive-ion mode ESI-MS spectra were measured with a Bruker (Billerica, MA, USA) micrOTOFII using sodium formate as a mass calibrant. Elemental analysis was performed

using a Yanaco (Tokyo, Japan) CHN corder MT-6 instrument at Shimane University. The infrared spectrum was measured with a JASCO (Tokyo, Japan) FT/IR-6300 spectrophotometer using a KBr disk. The temperature dependence of the magnetic susceptibility was measured with a Quantum Design (San Diego, CA, USA) MPMS-3 SQUID magnetometer at a magnetic field of 5000 Oe in the temperature range of 2–300 K. The absorption spectrum was measured using a JASCO (Tokyo, Japan) V-670 spectrophotometer. Diffuse reflectance spectra were recorded using a JASCO V-670 spectrophotometer equipped with an ISN-923 integrating sphere. Cyclic voltammetry (CV) measurement was performed with a scan rate of 100 mV/s in degassed propylene carbonate (PC) solution containing 0.10 M tetrabutylammonium hexafluorophosphate ($TBAPF_6$) using a HOKUTO DENKO (Tokyo, Japan) HZ-7000 system with a 3.0 mm glassy carbon disk, platinum wire, and saturated calomel electrode (SCE).

2.2. Synthesis of $[Ru_2(npc)_2(O_2CCF_3)_2]$ (**2**)

Complex **1** (67.6 mg, 0.100 mmol) was dissolved in trifluoroacetic acid (30.0 mL) and refluxed under nitrogen for 12 h. After cooling to room temperature, the solution was evaporated and then purified by silica gel column chromatography (eluent: 4:1 CH_2Cl_2–MeOH). The resultant solution was evaporated to dryness, and the obtained black powder was washed with diethyl ether (Et_2O) and dried under vacuum at 393 K for 3 h. Yield: 68.9 mg (0.0879 mmol, 87.9%). Anal. Calc. for $C_{22}H_{10}N_4O_8F_6Ru_2 \cdot 0.5H_2O$: C, 33.73; H, 1.41; N, 7.15%. Found: C, 33.82; H, 1.90; N, 7.08%. ESI-MS: calc. for $[M + Na]^+$: 798.8396 *m*/*z*; found 798.8393 *m*/*z*. FT-IR (cm^{-1}): 622 (w), 737 (m), 780 (m), 826 (vw), 864 (m), 916 (w), 1039 (w), 1158 (s), 1200 (vs), 1317 (w), 1352 (m), 1621 (vs), 1645 (vs), 3073 (w), 3431 (s).

2.3. Theoretical Calculation Methods

All DFT calculations in this study were performed using the uB3LYP functional [38], with the SDD basis set for Ru atoms, the aug-cc-pVDZ for N, O, and F atoms, and the cc-pVDZ basis set for other atoms, on the Gaussian 16 C.01 suite program [39–41]. This combination of functional method and basis sets theoretically reproduced the experimental results of **1** (molecular structure and absorption spectrum) well [32]. The polarizable continuum model was applied to consider the effect of *N*,*N*-dimethylformamide (DMF) [42]. Geometry optimization was conducted without symmetry constraints, and the obtained geometry was verified by frequency analysis. TDDFT calculation [43] was conducted to estimate the absorption wavelengths, oscillator strengths, and excitation characters.

2.4. Crystallography

Synchrotron SCXRD data of **2** was collected at 100 K using a Pilatus3 X CdTe 1M detector, and monochromated synchrotron radiation (λ = 0.4139 Å) installed at the BL02B1 beamline of the SPring-8 synchrotron radiation facility. Diffraction data were collected and processed using the CrysAlisPro program (version 1.171.42.94a) [44]. The structure was solved by the SHELXT program [45] with the intrinsic phasing method and then refined with full-matrix least squares on F^2 using the SHELXL program [46] in the Olex2 software (version 1.5) [47]. All non-hydrogen atoms were refined with anisotropic thermal parameters, and all hydrogen atoms were fixed at the calculated positions and refined as riding models. The electron densities of the disordered Et_2O solvents were removed using the Olex2 solvent mask. The crystallographic data for the final refined structure of **2** is summarized in Table 1, and the structural parameters of **2** are summarized in Table S1 in Supplementary Materials. The crystallographic data can be obtained free of charge from the Cambridge Crystallographic Data Centre (CCDC); deposition number of **2** is CCDC-2427167.

Table 1. Crystallographic data of **2**.

Complex	2
Radiation type	synchrotron
Radiation wavelength	0.4108
Chemical formula	$C_{24}H_{13}F_6N_5O_8Ru_2$
Formula weight	815.53
Crystal system	Tetragonal
Space group	$I\,4_1/a$
a (Å)	18.66850 (10)
b (Å)	18.66850 (10)
c (Å)	33.7511 (2)
α (deg)	90
β (deg)	90
γ (deg)	90
V (Å^3)	11,762.69 (14)
Z	16
D_{calc} (g cm^{-3})	1.842
μ (mm^{-1})	1.483
F (000)	6368
R_1 ($I > 2\sigma(I)$)	0.0379
wR_2 ($I > 2\sigma(I)$)	0.1062
R_1 (all data)	0.0384
wR_2 (all data)	0.1067
GOF on F^2	1.072

3. Results

3.1. Synthesis and Chatacterization

The synthetic scheme for complex **2** is shown in Scheme 2. By reacting **1** with an excess amount of trifluoroacetic acid under nitrogen for 12 h and purifying the resulting solution through silica-gel column chromatography, a black powder of **2** was obtained with a good yield of 87.9%. The resulting complex **2** was paramagnetic and remained stable in both solution and solid states in the air. **2** dissolved in common organic solvents such as CH_2Cl_2, $CHCl_3$, alcohols, DMF, and PC. Additionally, **1** was found to dissolve in tetrahydrofuran, whereas **2** did not.

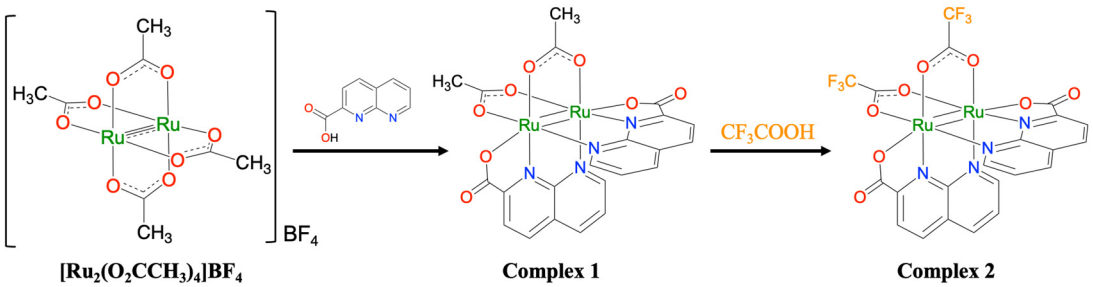

Scheme 2. Synthetic scheme for complex **2**.

The positive-ion ESI-MS spectrum of **2** displayed an intense signal at 798.8393 m/z, corresponding to the calculated $[M + Na]^+$ value of $[Ru_2(npc)_2(O_2CCF_3)_2]$ (798.8396 m/z). As shown in Figure 1, the observed isotope distribution pattern of **2** is consistent with the simulated pattern. No signal originating from the precursor complex **1** or the ligand exchange intermediate species of **2**, i.e., $[Ru_2(npc)_2(O_2CMe)(O_2CCF_3)]$, were observed. The CHN elemental analysis result of **2** showed good agreement with the calculated values for **2** with 0.5 H_2O. In the infrared spectrum (Figure S1), the asymmetric stretching modes

of the CO_2^- group, i.e., ν_{asym} (CO_2^-), of bridging $^-O_2CCF_3$ ligands in **2** was observed at 1644 cm^{-1}, which was consistent with that of $[Ru_2(O_2CCF_3)_4]$ (1624 cm^{-1}) [48]. In addition, the ν_{asym} (CO_2^-) of the carboxylate moieties of the npc ligands in **2** was found at 1620 cm^{-1}. Because the vibration mode of the carboxyl (COOH) group, which generally appears around 1700 cm^{-1} [49], was not found in the infrared spectrum of **2**, the carboxyl groups were understood to be fully deprotonated in **2**.

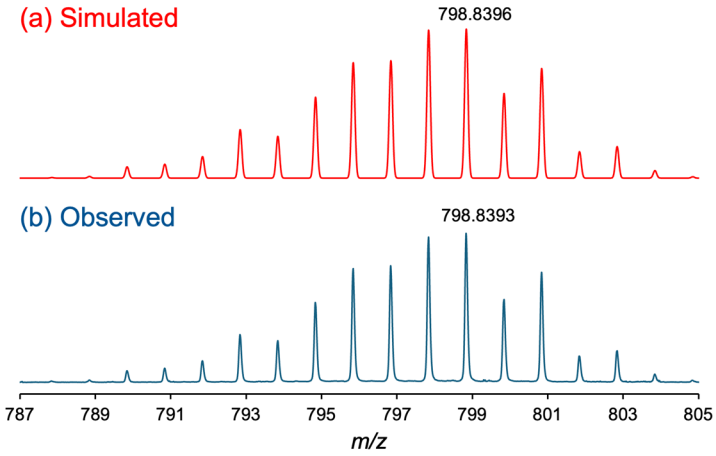

Figure 1. Isotope distribution patterns of (**a**) simulated and (**b**) observed ESI-MS spectra of **2**.

3.2. Crystal Structure

Single crystals of **2**, suitable for X-ray diffraction analyses, were obtained by slow diffusion of Et_2O into an acetonitrile solution of **2**. The diffraction analysis of a black block-shaped crystal of **2** was performed at 100 K using the high-energy synchrotron source at the BL02B1 beamline of the SPring-8 synchrotron facility in Japan, and this analysis revealed that **2** crystallized in the tetragonal system with the $I\,4_1/a$ space group. Figure 2 shows the crystal structure (thermal ellipsoid view) of **2** with a selected numbering scheme. Selected bond lengths and angles in **2** are summarized in Table S1.

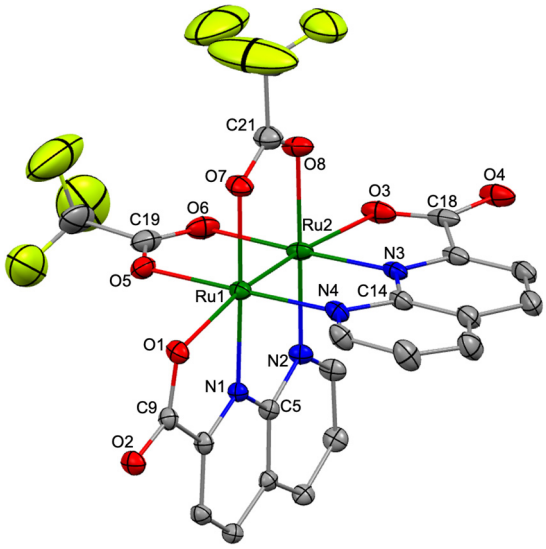

Figure 2. Crystal structure of **2** [Ru: green, C: gray, N: blue, O: red, and F: yellow]. Thermal ellipsoids were set at 30% probability level, and hydrogen atoms and solvent molecules are omitted for clarity.

The asymmetric unit of the crystal contained one crystallographically independent molecule of **2** and co-crystallized solvent molecules (one CH_3CN and one disordered Et_2O). The molecular structure of **2** formed the paddlewheel structure in which two npc and

two O_2CCF_3 bridging ligands were coordinated to the Ru_2 core in a *cis*-2:2 arrangement, similar to that of **1** [32]. The naphthyridine and carboxylate moieties in npc ligands were coordinated to the equatorial and axial positions of the Ru_2 core in **2**. The Ru–Ru bond length in **2** was 2.2978 (4) Å, which was slightly longer than those in **1** (2.2893 (4) Å) [32], $[Ru_2(O_2CCF_3)_4(THF)_2]$ (2.276 (3) Å) [48], and $[Ru_2(monp)_4]$ (2.258 (2) Å; monp = 7-methyl-1,8-naphthyridin-2-one) [50], indicating that a double bond was formed between the two Ru atoms in **2**. The averaged Ru–$N_{(npc)}$ and Ru–$O_{(npc)}$ bond lengths in **2** were 2.046 and 2.219 Å, respectively, which were slightly shorter than those in **1** (Ru–$N_{(npc)}$: 2.051 Å Ru–$O_{(npc)}$: 2.243 Å), whereas the average bridging Ru–O bond length in **2** was 2.087 Å, which was slightly longer than that in **1** (2.076 Å) [32].

3.3. Magnetic Properties

The magnetic susceptibility was measured at a magnetic field of 5000 Oe in the temperature range of 2–300 K to clarify the spin state and magnetic property of **2**. Figure 3 shows the temperature dependence of the molar magnetic susceptibility (χ_M) and effective moments (μ_{eff}) of **2**. At 300 K, the μ_{eff} value of **2** was estimated to be 2.73 μ_B, which aligned well with the spin-only value of 2.83 μ_B predicted for the triplet spin (S = 1) state of the Ru_2^{4+} complex, while it significantly deviated from the 3.87 μ_B predicted for the quartet spin (S = 3/2) state of the Ru_2^{5+} complex. With decreasing temperature, **2** exhibited a gradual increase in χ_M value and a corresponding decrease in μ_{eff} value. The χ_M and μ_{eff} values of **2** at 2.0 K reached 7.07 × 10^{-3} emu/mol and 0.34 μ_B, respectively.

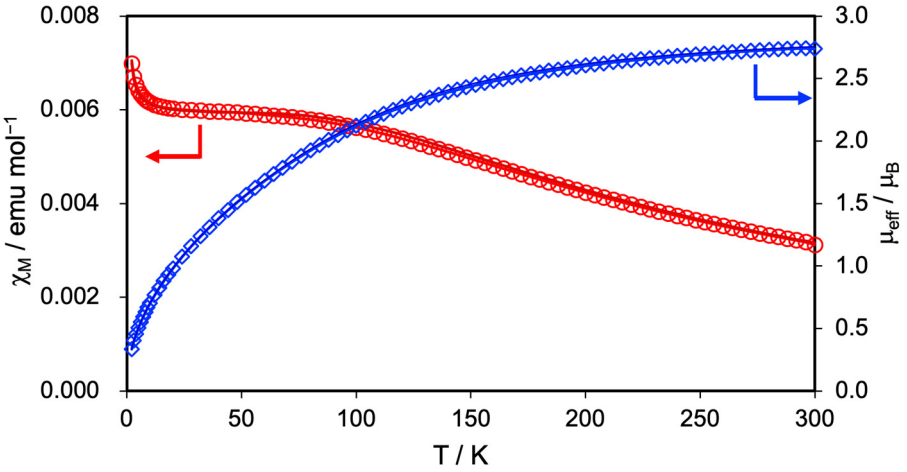

Figure 3. Temperature-dependent magnetic susceptibility (red circle) and effective magnetic moment (blue rhombus) of **2**. The solid lines represent the best fit of the data using Equation (1).

This magnetic behavior of **2** is similar to that of **1**, suggesting that zero-field splitting (ZFS) characteristics of the Ru_2 complexes occur [51,52]. Therefore, by fitting the measurement data of **2** using Equation (1), we determined the ZFS parameter (the D tensor) and g-value [53].

$$\chi_M = (1-\rho)\left[\frac{2N\beta^2 g^2}{3kT}\cdot\frac{\left\{e^{-\frac{D}{kT}}+\left(\frac{2kT}{D}\right)\left(1-e^{-\frac{D}{kT}}\right)\right\}}{\left(1+2e^{-\frac{D}{kT}}\right)}\right]+\rho\left(\frac{5N{g_{imp}}^2\beta^2}{4kT}\right) \quad (1)$$

In this equation, ρ is the correction term for a small amount of paramagnetic impurity with S = 1/2 (= 0.0012), N is the Avogadro's number, β is the Bohr magneton, k is the Boltzmann constant, and g_{imp} value is assumed to equal the average g-value. The best-fitting results indicated that **2** has a D tensor of 243 cm^{-1} and a g-value of 2.03. Table 2 summarizes the D tensor and g values of **1**, **2**, and related Ru_2 complexes. The D tensor of **2**

is close to those of **1** and other Ru_2^{4+} complexes such as $[Ru_2(O_2CMe)_4]$ (244 cm^{-1}) [54], $[Ru_2(O_2CCF_3)_4]$ (220 cm^{-1}) [37], and $[Ru_2(O_2CC_9H_{17})]$ (283 cm^{-1}) [55], but significantly different from those of Ru_2^{5+} complexes such as $[Ru_2(O_2CMe)_4(H_2O)_2]BPh_4$ (71.8 cm^{-1}) [56] and $[Ru_2(O_2CC_3H_7)_4Cl]$ (77 cm^{-1}) [57]. This result strongly supports that **2** adopts an oxidation state of Ru_2^{4+} with $S = 1$.

Table 2. *D* tensors and g-values of **1**, **2**, and related Ru_2 complexes.

Complex	*D* Tensor (cm^{-1})	*g* Value	Ref
1	227	2.13	32
2	243	2.03	this study
$[Ru_2(O_2CMe)_4]$	244	2.08	54
$[Ru_2(O_2CCF_3)_4]$	220	2.0	37
$[Ru_2(O_2CC_9H_{17})]$	283	—	55
$[Ru_2(O_2CMe)_4(H_2O)_2]BPh_4$	72	2.19	56
$[Ru_2(O_2CC_3H_7)_4Cl]$	77	2.10	57

3.4. Optimized Geometry and Electronic Structure

Unrestricted DFT calculations were performed to gain a deeper understanding of the molecular geometry and electronic structure of **2**. The results of full geometry optimization indicated that the optimized geometry of **2** adopts a paddlewheel-type structure with a *cis*-2:2 arrangement, consistent with the experimental structure. The optimized Ru–Ru bond length in **2** was 2.337 Å, which was only 0.04 Å longer than the experimental value (2.2978 (4) Å). Additionally, as shown in Table S2, the averaged bond lengths between the Ru_2 core and the primary coordination sphere [Ru–$N_{(npc)}$, Ru–$O_{(npc)}$, and Ru–$O_{(O_2CCF_3)}$] in the optimized geometry of **2** were approximately 0.01 to 0.04 Å longer than the experimental values. The slight elongation of these bond lengths in the optimized geometry compared with the crystal structure is likely due to the absence of crystal packing stress [58].

Figure 4 depicts the MO diagrams near the frontier MOs, as well as the HOMOs and LUMOs of **1** and **2**. The occupied MO features of **2** are very similar to those of **1**, but the orbital energies of **2** are relatively more stabilized than those of **1**. Specifically, the two singly unoccupied MOs, i.e., HOMO (α) and HOMO-1 (α), of **2** are localized on the π* (Ru_2) orbitals and are stabilized by 0.30 and 0.39 eV, respectively, compared with those of **1**. The δ* (Ru_2) orbitals were observed in HOMO-2 (α) and HOMO (β), while the σ (Ru_2) orbitals, which are the most unstable bonding d–d orbital interaction, were found in HOMO-3 (α) and HOMO-1 (β). The HOMO (α) and HOMO (β) orbitals of **2** were stabilized by 0.40 and 0.42 eV, respectively, compared with those of **1**. In the unoccupied MO spaces, clear differences in orbital stability were observed between **1** and **2** due to the electron-withdrawing effect of the O_2CCF_3 ligands; while the π* (npc) orbitals of **2** were also stabilized by the electron-withdrawing nature of the O_2CCF_3 ligands, the energy differences between **1** and **2** were relatively smaller than those of π* (Ru_2) orbital. Consequently, although LUMO (α) was localized on the π* (npc) orbitals in both complexes, the LUMO (β) orbital in **1** was localized on the π* (npc) orbital, while the LUMO (β) orbital in **2** was localized on the π* (Ru_2) orbital (see Figure 4b). Based on the results of these MO analyses, the electronic configurations between two Ru ions in **2** can be described as $\pi^4\delta^2\sigma^2\delta^{*2}\pi^{*2}$, which is the same as the case of **1** [32].

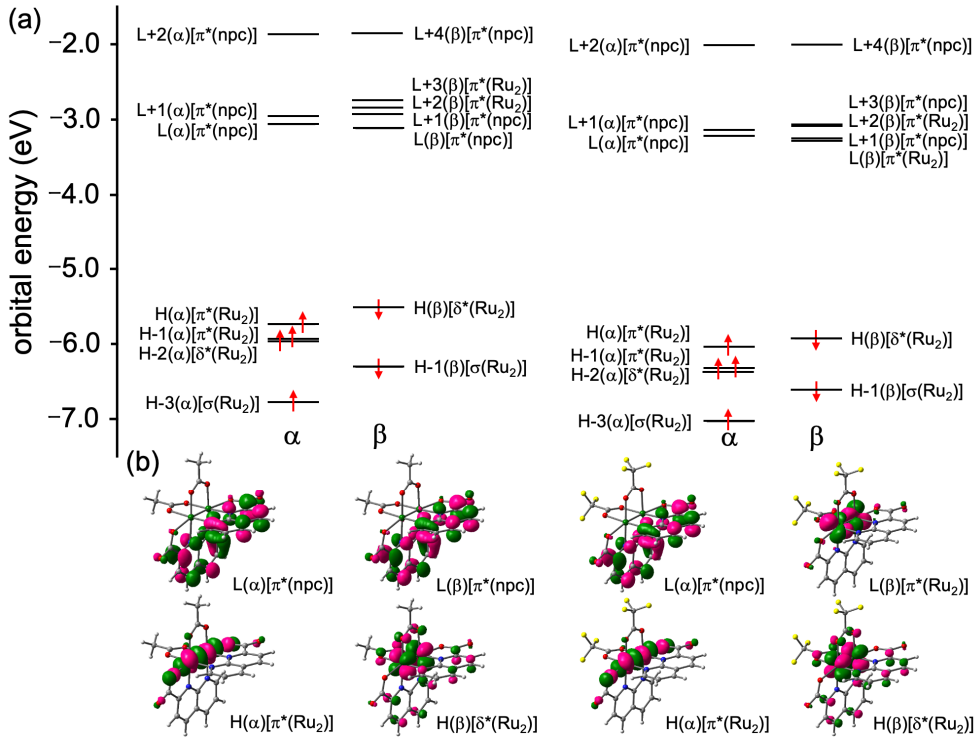

Figure 4. (**a**) MO diagrams and (**b**) HOMOs [H] and LUMOs [L] of **1** and **2**.

3.5. Electrochemical Property

CV measurement was performed in a degassed PC solution containing 0.10 M $TBAPF_6$ to investigate the electrochemical properties of **2**. The obtained redox potential ($E_{1/2}$) and the separation of the oxidation and reduction waves (DE) are summarized in Table S4. As shown in Figure 5, **2** exhibited one reversible wave at $E_{1/2}$ = 0.72 V vs. SCE on the oxidation side and two reversible waves at $E_{1/2}$ = −0.67 and −1.10 V vs. SCE on the reduction side. The CV diagram of **2** was similar to that of **1**, but the $E_{1/2}$ values of **2** were shifted in the positive direction relative to those of **1** ($E_{1/2}$ = 0.43, −0.92, and −1.19 V vs. SCE) [32]. This large positive shift of **2** originated from the electron-withdrawing effect of the two O_2CCF_3 ligands and is consistent with the stabilization of the HOMO (α) orbital of **2** compared to that of **1**. Further, **2** was easily oxidized compared with $[Ru_2(O_2CCF_3)_4]$ ($E_{1/2}$ = 1.8 V vs. SCE) [59]. From the results of the electronic structure of **2** calculated by DFT and CV result of Hnpc ($E_{1/2}$ = −0.91 V vs. SCE; Figure S2), the oxidation wave was attributed to the Ru_2^{5+}/Ru_2^{4+} process, while the two reduction waves were associated with the reduction of two npc ligands (i.e., npc/npc^- processes).

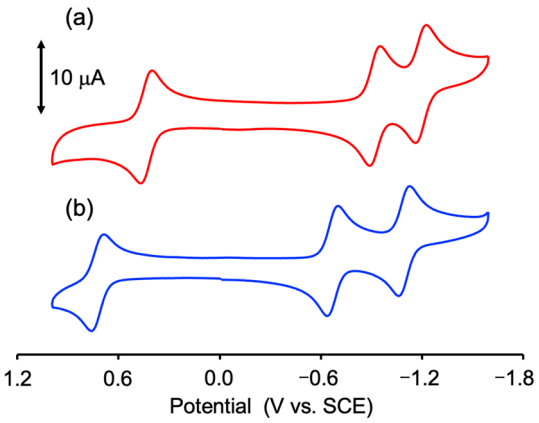

Figure 5. CV diagrams of (**a**) **1** [red line] and (**b**) **2** [blue line] in degassed PC/$TBAPF_6$.

3.6. Absorption-Spectral Property

The steady-state absorption spectrum of **2** was measured in DMF at 300 K. As shown in Figure 6, **2** displayed intense absorption bands in the visible light region similar to those of **1** but with a clear blue shift [32]. Specifically, **2** exhibited a shoulder band around 680–700 nm and an intense band at 555 nm (ε = 3780 $M^{-1}cm^{-1}$). The absorption bands of **2** were found to be blue-shifted by approximately 70–100 nm when the absorption bands of **2** were compared with the corresponding bands of **1**. The significant blue shift of these absorption bands in **2** was considered to be due to the electron-withdrawing effect of trifluoroacetate ligands in **2**. As shown in Table S3, TDDFT calculations revealed that the main contributions of the shoulder and intense bands of **2** in the visible light region are MLCTs from the δ^* (Ru_2) to the π^* (npc) orbitals. Additionally, the d–d transitions and MLCTs from the π^* (Ru_2), σ (Ru_2), or δ (Ru_2) to the π^* (npc) orbitals are also involved as minor contributions in their absorption bands. Therefore, the blue shift in the absorption bands of **2** compared with that of **1** was concluded to originate from the stabilization of δ^* (Ru_2) orbital in **2** due to the electron-withdrawing effect of the CF_3COO^- ligands. The absorption bands in the solid-state diffuse reflectance spectra of **1** and **2** appear at approximately the same positions as those in solution (see Figure S3).

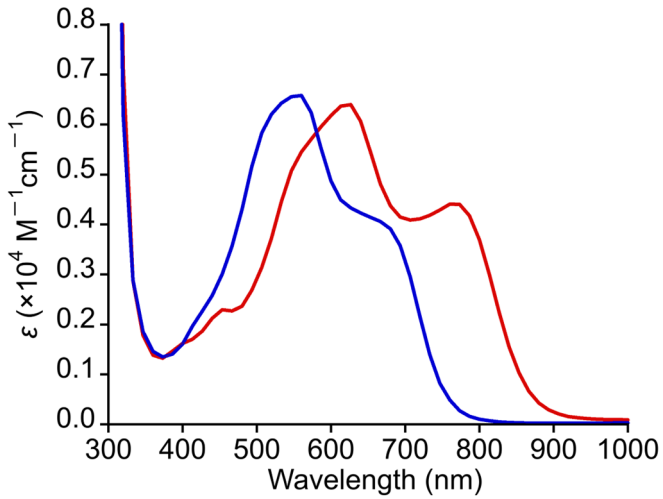

Figure 6. Absorption spectra of **1** (red line) and **2** (blue line) in DMF.

4. Conclusions

A new paddlewheel-type Ru_2 naphthyridine complex with two trifluoroacetate ligands, $[Ru_2(npc)_2(O_2CCF_3)_2]$ (**2**), was synthesized and structurally characterized. SCXRD analyses revealed that **2** adopted a paddlewheel-type structure, in which two npc ligands and two O_2CCF_3 ligands were coordinated in a *cis*-2:2 arrangement around the Ru_2 core. The Ru–Ru and average bridging Ru–O bond lengths in **2** were 2.2978(4) and 2.087 Å, which were slightly longer than those in **1** (2.2893 (4) and 2.076 Å, respectively), whereas the averaged $Ru–N_{(npc)}$ and $Ru–O_{(npc)}$ bond lengths in **2** were 2.046 and 2.219 Å, respectively, which were slightly shorter than those in **1** ($Ru–N_{(npc)}$: 2.051 Å $Ru–O_{(npc)}$: 2.243 Å). Based on the results from magnetic susceptibility measurements and DFT calculations, **2** had a Ru^{2+} oxidation state and possessed unpaired spins in the two $\pi^*(Ru_2)$ orbitals, resulting in a spin state of S = 1. The paddlewheel-type Ru_2^{4+} complex was generally unstable in the air; however, **2** was a rare compound that remained stable in both solid and solution states. As expected, **2** was a redox-active compound and exhibited MLCT transitions from the Ru_2 core to the npc ligands in the visible light region; (i) the absorption bands of **2** were found to be blue-shifted by approximately 70–100 nm relative to those of **1**, and (ii) the $E_{1/2}$ values of **2** ($E_{1/2}$ = 0.72, −0.67 and −1.10 V vs. SCE) were shifted in the positive direction relative

to those of **1** ($E_{1/2}$ = 0.43, −0.92, and −1.19 V vs. SCE). This study has revealed that the absorption band positions and redox potentials of the Ru_2 naphthyridine complex could be modified through the appropriate selection of bridging carboxylate ligands. We are planning to carry out further research on the development of electrochromic [28] and/or supramolecular complexes [60,61] using this Ru_2 core structure.

Supplementary Materials: The following supporting information can be downloaded at: https://www.mdpi.com/article/10.3390/chemistry7030072/s1, Figure S1: Infrared spectrum of **2**.; Figure S2: CV diagram of Hnpc (1.0 mM) in PC/$TBAPF_6$.; Figure S3: Diffuse reflectance spectra of **1** (red line) and **2** (blue line).; Table S1: Selected bond lengths (Å) and angles (°) of crystal structure of **2**.; Table S2: Averaged bond lengths between the Ru_2 core and the primary coordination sphere in the crystal structure and optimized geometry of **2**.; Table S3: TDDFT results (absorption wavelengths, oscillator strengths (*f*), and assignments of excitation character) for **2**.; Table S4: Redox potentials ($E_{1/2}$; V vs. SCE) and the separation of the oxidation and reduction waves (ΔE; mV) of **1** and **2**.

Author Contributions: Conceptualization, Y.K.; Validation, Y.K., N.Y. and M.H.; Formal analysis, Y.K., N.T., J.O., K.M., N.Y. and M.H.; Investigation, Y.K., N.T., J.O., K.M. and N.Y.; Resources, Y.K., N.Y. and M.H.; Data curation, Y.K., N.Y. and M.H.; Writing—original draft preparation, Y.K.; Writing—review and editing, Y.K., N.T., J.O., K.M., N.Y. and M.H.; Visualization, Y.K. and N.Y.; Supervision, Y.K.; Project administration, Y.K.; Funding acquisition, Y.K. All authors have read and agreed to the published version of the manuscript.

Funding: This research was funded by the Japan Society for the Promotion of Science (JSPS KAKENHI; Grant Number 24K08494, 22K14765, and 24K08363) and SDGs research project of Shimane University.

Data Availability Statement: Data are contained within the article or Supplementary Materials.

Acknowledgments: The synchrotron radiation experiments were performed at the BL02B1 of SPring–8 with the approval of the Japan Synchrotron Radiation Research Institute (JASRI) (Proposal No. 2022B1647, 2023A1741, 2023B1829, 2024A1713, and 2024B1920).

Conflicts of Interest: The authors declare no conflicts of interest.

References

1. Cotton, F.A.; Murillo, C.A.; Walton, R.A. *Multiple Bonds Between Metal Atoms*, 3rd ed.; Springer Science and Business Media: New York, NY, USA, 2005.
2. Chisholm, M.H.; Patmore, N.J. Studies of electronic coupling and mixed valency in metal-metal quadruply bonded complexes linked by dicarboxylate and closely related ligands. *Acc. Chem. Res.* **2007**, *40*, 19–27. [CrossRef] [PubMed]
3. Murillo, C.A. Adventures in Divalent Early Transition Metal Coordination Chemistry: On the Way to Metal–Metal Bonded Species. *Inorg. Chim. Acta* **2017**, *468*, 3–15. [CrossRef]
4. Ren, T. Substituent Effects in Dinuclear Paddlewheel Compounds: Electrochemical and Spectroscopic Investigations. *Coord. Chem. Rev.* **1998**, *175*, 43–58. [CrossRef]
5. Hrdina, R. Dirhodium(II,II) Paddlewheel Complexes. *Eur. J. Inorg. Chem.* **2021**, *6*, 501–528. [CrossRef]
6. Köberl, M.; Cokoja, M.; Herrmann, W.A.; Kühn, F.E. From Molecules to Materials: Molecular Paddle-Wheel Synthons of Macromolecules, Cage Compounds, and Metal–Organic Frameworks. *Dalton Trans.* **2011**, *40*, 6834–6859. [CrossRef] [PubMed]
7. Kataoka, Y.; Yano, N.; Mikuriya, M.; Handa, M. Paddlewheel-type dirhodium complexes with N,N′-bridging ligands. *Coord. Chem. Rev.* **2023**, *479*, 214997. [CrossRef]
8. Li, H.; Eddaoudi, M.; Groy, T.L.; Yaghi, O.M. Establishing Microporosity in Open Metal–Organic Frameworks: Gas Sorption Isotherms for Zn(BDC) (BDC = 1,4-Benzenedicarboxylate). *J. Am. Chem. Soc.* **1998**, *120*, 8571–8572. [CrossRef]
9. Dybtsev, D.N.; Chun, H.; Kim, K. Rigid and Flexible: A Highly Porous Metal–Organic Framework with Unusual Guest-Dependent Dynamic Behavior. *Angew. Chem. Int. Ed.* **2004**, *43*, 5033–5036. [CrossRef]
10. Mori, W.; Takamizawa, S.; Nozaki Kato, C.; Ohmura, T.; Sato, T. Molecular-Level Design of Efficient Microporous Materials Containing Metal Carboxylates: Inclusion Complex Formation with Organic Polymer, Gas-Occlusion Properties, and Catalytic Activities for Hydrogenation of Olefins. *Microporous Mesoporous Mater.* **2004**, *73*, 31–46. [CrossRef]
11. Miyasaka, H. Charge Manipulation in Metal–Organic Frameworks: Toward Designer Functional Molecular Materials. *Bull. Chem. Soc. Jpn.* **2021**, *94*, 2929–2955. [CrossRef]

12. Kataoka, Y.; Yano, N.; Mikuriya, M.; Handa, M. Coordination polymers and metal–organic frameworks based on paddlewheel-type dirhodium(II) tetracarboxylates. *Coord. Chem. Rev.* **2022**, *472*, 214796. [CrossRef]
13. Aquino, M.A.S. Diruthenium and Diosmium Tetracarboxylates: Synthesis, Physical Properties, and Applications. *Coord. Chem. Rev.* **1998**, *170*, 141–202. [CrossRef]
14. Aquino, M.A.S. Recent Developments in the Synthesis and Properties of Diruthenium Tetracarboxylates. *Coord. Chem. Rev.* **2004**, *248*, 1025–1045. [CrossRef]
15. Van Caemelbecke, E.; Phan, T.; Osterloh, W.R.; Kadish, K.M. Electrochemistry of Metal-Metal Bonded Diruthenium Complexes. *Coord. Chem. Rev.* **2021**, *434*, 213706. [CrossRef]
16. Cortijo, M.; González-Prieto, R.; Herrero, S.; Priego, J.L.; Jiménez-Aparicio, R. The Use of Amidinate Ligands in Paddlewheel Diruthenium Chemistry. *Coord. Chem. Rev.* **2019**, *400*, 213040. [CrossRef]
17. Mikuriya, M.; Yoshioka, D.; Handa, M. Magnetic Interactions in One-, Two-, and Three-Dimensional Assemblies of Dinuclear Ruthenium Carboxylates. *Coord. Chem. Rev.* **2006**, *250*, 2194–2211. [CrossRef]
18. Liao, Y.; Shum, W.W.; Miller, J.S. Synthesis and Magnetic Properties of 3-D $[Ru^{II/III}{}_2(O_2CMe)_4]_3[M^{III}(CN)_6]$ (M = Cr, Fe, Co). *J. Am. Chem. Soc.* **2002**, *124*, 9336–9337. [CrossRef]
19. Angaridis, P.; Cotton, F.A.; Murillo, C.A.; Villagrán, D.; Wang, X. Structural and Magnetic Evidence Concerning Spin Crossover in Formamidinate Compounds with $Ru_2{}^{5+}$ Cores. *J. Am. Chem. Soc.* **2005**, *127*, 5008–5009. [CrossRef]
20. Miyasaka, H.; Motokawa, N.; Matsunaga, S.; Yamashita, M.; Sugimoto, K.; Mori, T.; Toyota, N.; Dunbar, K.R. Control of Charge Transfer in a Series of $Ru_2{}^{2+}$/TCNQ Two-Dimensional Networks by Tuning the Electron Affinity of TCNQ Units: A Route to Synergistic Magnetic/Conducting Materials. *J. Am. Chem. Soc.* **2010**, *132*, 1532–1544. [CrossRef]
21. Zhang, J.; Kosaka, W.; Liu, Q.; Amamizu, N.; Kitagawa, Y.; Miyasaka, H. CO_2-Sensitive Porous Magnet: Antiferromagnet Creation from a Paramagnetic Charge-Transfer Layered Metal–Organic Framework. *J. Am. Chem. Soc.* **2023**, *145*, 26179–26189. [CrossRef]
22. Trenerry, M.J.; Wallen, C.M.; Brown, T.R.; Park, S.V.; Berry, J.F. Spontaneous N_2 Formation by a Diruthenium Complex Enables Electrocatalytic and Aerobic Oxidation of Ammonia. *Nat. Chem.* **2021**, *13*, 1221–1227. [CrossRef] [PubMed]
23. Kataoka, Y.; Sato, K.; Miyazaki, Y.; Masuda, K.; Tanaka, H.; Naito, S.; Mori, W. Photocatalytic Hydrogen Production from Water Using Porous Material $[Ru_2(p\text{-BDC})_2]_n$. *Energy Environ. Sci.* **2009**, *2*, 397–400. [CrossRef]
24. Miyazawa, T.; Suzuki, T.; Kumagai, Y.; Takizawa, K.; Kikuchi, T.; Kato, S.; Onoda, A.; Hayashi, T.; Kamei, Y.; Kamiyama, F.; et al. Chiral Paddle-Wheel Diruthenium Complexes for Asymmetric Catalysis. *Nature Catal.* **2020**, *3*, 851–858. [CrossRef]
25. Villalobos, L.; Barker Paredes, J.E.; Cao, Z.; Ren, T. *tert*-Butyl Hydroperoxide Oxygenation of Organic Sulfides Catalyzed by Diruthenium(II,III) Tetracarboxylates. *Inorg. Chem.* **2013**, *52*, 12545–12552. [CrossRef]
26. Tolbatov, I.; Barresi, E.; Taliani, S.; La Mendola, D.; Marzo, T.; Marrone, A. Diruthenium(II,III) Paddlewheel Complexes: Effects of Bridging and Axial Ligands on Anticancer Properties. *Inorg. Chem. Front.* **2023**, *10*, 2226–2238. [CrossRef]
27. Barresi, E.; Tolbatov, I.; Marzo, T.; Zappelli, E.; Marrone, A.; Re, N.; Pratesi, A.; Martini, C.; Taliani, S.; Da Settimo, F.; et al. Two Mixed-Valence Diruthenium(II,III) Isomeric Complexes Show Different Anticancer Properties. *Dalton Trans.* **2021**, *50*, 9643–9647. [CrossRef]
28. Kataoka, Y.; Imasaki, N.; Yano, N.; Mitsumi, M.; Handa, M. Redox-Triggered Reversible Modulation of Intense Near-Infrared and Visible Absorption Using Paddlewheel-Type Diruthenium(III) Complex. *Dalton Trans.* **2021**, *50*, 9547–9553. [CrossRef]
29. Stephenson, T.A.; Wilkinson, G. New Ruthenium Carboxylate Complexes. *J. Inorg. Nucl. Chem.* **1966**, *28*, 2285–2291. [CrossRef]
30. Lindsay, A.J.; Tooze, R.P.; Motevalli, M.; Hursthouse, M.B.; Wilkinson, G. The Synthesis and Structure of Tetra-μ-acetatodiruthenium(II,II)–bis(tetrahydrofuran). *J. Chem. Soc. Chem. Commun.* **1984**, *20*, 1383b–1384. [CrossRef]
31. Furukawa, S.; Kitagawa, S. Neutral Paddlewheel Diruthenium Complexes with Tetracarboxylates of Large π-Conjugated Substituents: Facile One-Pot Synthesis, Crystal Structures, and Electrochemical Studies. *Inorg. Chem.* **2004**, *43*, 6464–6472. [CrossRef]
32. Kataoka, Y.; Tada, N.; Masamori, N.; Yano, N.; Moriyoshi, C.; Handa, M. Paddlewheel-Type and Half-Paddlewheel-Type Diruthenium(II,II) Complexes with 1,8-Naphthyridine-2-Carboxylate. *Dalton Trans.* **2025**, *54*, 3047–3056. [CrossRef]
33. Miyasaka, H.; Motokawa, N.; Atsuumi, R.; Kamo, H.; Asai, Y.; Yamashita, M. Tuning of the Ionization Potential of Paddlewheel Diruthenium(II,II) Complexes with Fluorine Atoms on the Benzoate Ligands. *Dalton Trans.* **2011**, *40*, 673–682. [CrossRef] [PubMed]
34. Kosaka, W.; Watanabe, Y.; Aliyah, K.H.; Miyasaka, H. Role of Intramolecular Hydrogen Bonding in the Redox Chemistry of Hydroxybenzoate-Bridged Paddlewheel Diruthenium(II,II) Complexes. *Dalton Trans.* **2022**, *51*, 85–94. [CrossRef] [PubMed]
35. Lindsay, A.J.; Wilkinson, G.; Motevalli, M.; Hursthouse, M.B. The Synthesis, Magnetic, Electrochemical, and Spectroscopic Properties of Diruthenium(II,II) Tetra-μ-carboxylates and Their Adducts. X-Ray Structures of $Ru_2(O_2CR)_4L_2$ (R = Me, L = H_2O or Tetrahydrofuran; R = Et, L = Me_2CO). *J. Chem. Soc. Dalton Trans.* **1985**, *11*, 2321–2326. [CrossRef]
36. Barral, M.C.; Jimenez-Aparicio, R.; Royer, E.C.; Ruiz-Valero, C.; Urbanos, F.A.; Gutierrez-Puebla, E.; Monge, A. Tertiary Phosphine Oxide Adducts of Diruthenium(II,III) Tetraacetate. Crystal Structure of $[Ru_2(\mu\text{-}O_2CCH_3)_4(OPPh_3)_2]PF_6 \cdot CH_2ClCH_2Cl$. *Polyhedron* **1989**, *8*, 2571–2576. [CrossRef]

37. Dikarev, E.V.; Filatov, A.S.; Clérac, R.; Petrukhina, M.A. Unligated Diruthenium(II,II) Tetra(trifluoroacetate): The First X-ray Structural Study, Thermal Compressibility, Lewis Acidity, and Magnetism. *Inorg. Chem.* **2006**, *45*, 744–751. [CrossRef] [PubMed]
38. Becke, A.D. Density-Functional Thermochemistry. III. The Role of Exact Exchange. *J. Chem. Phys.* **1993**, *98*, 5648–5652. [CrossRef]
39. Andrae, D.; Haeussermann, U.; Dolg, M.; Stoll, H.; Preuss, H. Energy-Adjusted Ab Initio Pseudopotentials for the Second and Third Row Transition Elements. *Theor. Chem. Acc.* **1990**, *77*, 123–141. [CrossRef]
40. Dunning, T.H., Jr. Gaussian Basis Sets for Use in Correlated Molecular Calculations. I. The Atoms Boron through Neon and Hydrogen. *J. Chem. Phys.* **1989**, *90*, 1007–1023. [CrossRef]
41. Frisch, M.J.; Trucks, G.W.; Schlegel, H.B.; Scuseria, G.E.; Robb, M.A.; Cheeseman, J.R.; Scalmani, G.; Barone, V.; Petersson, G.A.; Nakatsuji, H.; et al. *Gaussian 16, Revision C.01*; Gaussian, Inc.: Wallingford, CT, USA, 2016.
42. Tomasi, J.; Mennucci, B.; Cammi, R. Quantum Mechanical Continuum Solvation Models. *Chem. Rev.* **2005**, *105*, 2999–3093. [CrossRef]
43. Adamo, C.; Jacquemin, D. The Calculations of Excited-State Properties with Time-Dependent Density Functional Theory. *Chem. Soc. Rev.* **2013**, *42*, 845–856. [CrossRef] [PubMed]
44. *CrysAlisPro Software System*; Rigaku Oxford Diffraction: Tokyo, Japan, 2018.
45. Sheldrick, G.M. SHELXT—Integrated space-group and crystal-structure determination. *Acta Cryst.* **2015**, *A71*, 3–8. [CrossRef] [PubMed]
46. Sheldrick, G.M. Crystal structure refinement with SHELXL. *Acta Cryst.* **2015**, *C71*, 3–8.
47. Dolomanov, O.V.; Bourhis, L.J.; Gildea, R.J.; Howard, J.A.K.; Puschmann, H. OLEX2: A complete structure solution, refinement and analysis program. *J. Appl. Cryst.* **2009**, *42*, 339–341. [CrossRef]
48. Lindsay, A.J.; Wilkinson, G.; Motevalli, M.; Hursthouse, M.B. Reactions of Tetra-μ-carboxylato-diruthenium(II,II) Compounds. X-Ray Crystal Structures of $Ru_2(\mu\text{-}O_2CCF_3)_4(THF)_2$, $Ru_2(\mu\text{-}O_2CR)_4(NO)_2$ (R = Et or CF_3), and $\{Na_3[Ru_2(\mu\text{-}O_2CO)_4]\cdot 6H_2O\}_n$. *J. Chem. Soc. Dalton Trans.* **1987**, *11*, 2723–2736. [CrossRef]
49. Nakamoto, K. *Infrared and Raman Spectra of Inorganic and Coordination Compounds, Part B: Applications in Coordination, Organometallic, and Bioinorganic Chemistry*, 6th ed.; John Wiley & Sons: Hoboken, NJ, USA, 2009.
50. Sheldrick, W.S.; Mintert, M. Dimolybdenum(II) and Diruthenium(II) Complexes with 2-Substituted 7-Methyl-1,8-Naphthyridines as Bridging Ligands. *Inorg. Chim. Acta* **1994**, *219*, 23–29. [CrossRef]
51. Shum, W.W.; Liao, Y.; Miller, J.S. Zero-Field Splitting, Field-Dependent Magnetization of Mixed-Valent S = 3/2 Diruthenium(II,III) Tetracarboxylates. *J. Phys. Chem. A* **2004**, *108*, 7460–7462. [CrossRef]
52. Chen, W.-Z.; Cotton, F.A.; Dalal, N.S.; Murillo, C.A.; Ramsey, C.M.; Ren, T.; Wang, X. Proof of Large Positive Zero-Field Splitting in a Ru_2^{5+} Paddlewheel. *J. Am. Chem. Soc.* **2005**, *127*, 12691–12696. [CrossRef]
53. Kataoka, Y.; Mikami, S.; Sakiyama, H.; Mitsumi, M.; Kawamoto, T.; Handa, M. A Neutral Paddlewheel-Type Diruthenium(III) Complex with Benzamidinato Ligands: Synthesis, Crystal Structure, Magnetism, and Electrochemical and Absorption Properties. *Polyhedron* **2017**, *136*, 87–92. [CrossRef]
54. Cotton, F.A.; Miskowski, V.M.; Zhong, B. Chemistry, Structure, and Bonding in Diruthenium(II) Tetracarboxylates. *J. Am. Chem. Soc.* **1989**, *111*, 6177–6182. [CrossRef]
55. Bonnet, L.; Cukiernik, F.D.; Maldivi, P.; Giroud-Godquin, A.-M.; Marchon, J.-C. Synthesis, X-Ray Diffraction, Differential Scanning Calorimetry, and Magnetic Susceptibility Studies of a Series of Binuclear Ruthenium(II) Carboxylates Giving Liquid-Crystalline Phases. *Chem. Mater.* **1994**, *6*, 31–38. [CrossRef]
56. Cukiernik, F.D.; Giroud-Godquin, A.-M.; Maldivi, P.; Marchon, J.-C. Pyrazine-Mediated Antiferromagnetic Intermolecular Exchange in Mixed-Valent Diruthenium Tetracarboxylates. *Inorg. Chim. Acta* **1994**, *215*, 203. [CrossRef]
57. Telser, J.; Drago, R.S. Reinvestigation of the Electronic and Magnetic Properties of Ruthenium Butyrate Chloride. *Inorg. Chem.* **1984**, *23*, 3114–3120. [CrossRef]
58. Kataoka, Y.; Sato, K.; Yano, N.; Handa, M. Ferrocene-Bearing Homoleptic and Heteroleptic Paddlewheel-Type Dirhodium Complexes. *Inorganics* **2024**, *12*, 41. [CrossRef]
59. Das, K.; Kadish, K.M.; Bear, J.L. Substituent and Solvent Effects on the Electrochemical Properties of Tetra-μ-carboxylato-dirhodium(II). *Inorg. Chem.* **1978**, *17*, 930–934. [CrossRef]
60. Angaridis, P.; Berry, J.F.; Cotton, F.A.; Murillo, C.A.; Wang, X. Molecular Squares with Paramagnetic Diruthenium Corners: Synthetic and Crystallographic Challenges. *J. Am. Chem. Soc.* **2003**, *125*, 10327–10334. [CrossRef]
61. Barral, M.C.; Gallo, T.; Herrero, S.; Jiménez-Aparicio, R.; Torres, M.R.; Urbanos, F.A. Equatorially Connected Diruthenium(II,III) Units toward Paramagnetic Supramolecular Structures with Singular Magnetic Properties. *Inorg. Chem.* **2006**, *45*, 3639–3647. [CrossRef]